Acta Metall. Sin. (Engl. Lett.), 2017, **30**(9), 840–850
DOI 10.1007/s40195-017-0599-y

Micromechanical Analysis of In-Plane Constraint Effect on Local Fracture Behavior of Cracks in the Weakest Locations of Dissimilar Metal Welded Joint

Jie Yang[1]

Received: 14 December 2016 / Revised: 22 January 2017 / Published online: 27 May 2017

Abstract In this work, a set of GTN (Gurson–Tvergaard–Needleman) parameters of the Alloy52M dissimilar metal welded joint (DMWJ) have been calibrated, and a micromechanical analysis of in-plane constraint effects on the local fracture behavior of two cracks, which located in the weakest regions of the DMWJ, has been investigated by the local approach based on the GTN damage model. The results show that the partition of the material and the variation of the q_2 parameter make the *J*-resistance curves obtained by numerical simulations close to the experimental values. The numerical *J*-resistance curves and crack growth paths are consistent with the experiment results, which show that the GTN damage model can incorporate the in-plane constraint effect. Furthermore, after the stress, strain and damage fields at the crack tip during the crack propagation process have been calculated, and the change of the *J*-resistance curves, crack growth paths and fracture mechanism with in-plane constraint have been analyzed.

KEY WORDS: Micromechanical analysis; In-plane constraint; Fracture behavior; Dissimilar metal welded joint; GTN (Gurson–Tvergaard–Needleman) damage model

1 Introduction

The dissimilar metal weld joint (DMWJ) is an indispensable part of the nuclear power plants (NPPs) and has been widely used in the primary water systems for connecting the pipe-nozzle to the safe end. But due to the harsh service environment and the highly heterogeneity of microstructure, mechanical and fracture properties, the DMWJ is also the vulnerable component of the NPPs. Different types of defects such as axial and circumferential defects have been found in the DMWJ [1, 2], and serious leakage events were reported [3, 4]. Thus, the DMWJ was treated as a key component of design, fabrication, inspection and monitoring in many countries, and the IAEA (International Atomic Energy Agency) Safety Standards pointed that the reasonable evaluation of the DMWJ is one of the key factors for the safe operation of the NPPs [5].

However, in the present integrity assessment methods, the particular assessment method for the DMWJ has not yet been provided. The joint is often simplified as a sandwich composite composed of base metal and weld metal; the interface region and heat-affected-zone (HAZ) are ignored. But the recent studies showed that the heat flow and element migration during welding process led to the complex microstructures and sharp fluctuation of mechanical property in the interface regions and HAZ, the ignored zone with the lowest *J*-resistance curves were the weakest locations of the DMWJ [6–8].

On the other hand, the complex geometry structures of the safe end are often simplified as a straight pipe in the present integrity assessment methods, and the effect of crack-tip constraint has not been taken into account

Available online at http://link.springer.com/journal/40195.

✉ Jie Yang
yangjie@usst.edu.cn

[1] School of Energy and Power Engineering, University of Shanghai for Science and Technology, Shanghai 200093, China

accurately. Constraint is the resistance of structure against plastic deformation [9]. According to the crack plane, it can be divided into two conditions of in-plane and out-of-plane. The in-plane constraint relates to the specimen dimension in the direction of growing crack, while the out-of-plane constraint relates to the specimen dimension parallel to the crack front. The loss of constraint can increase the load-bearing capacity of the cracked components. In the DMWJ, both in-plane and out-of-plane constraints generally exist. Thus, the simplified method can result in too conservative or non-conservative results inevitably.

Therefore, it is critical and essential to develop an accurate structural integrity assessment method, which considers the constraint, complex microstructures and the sharp fluctuation of mechanical property for the DMWJ. For this, the fracture behavior of cracks with different constraints which located in the weakest locations of the DMWJ needs to be clarified firstly.

In previous study, the fracture behavior of cracks located in various locations of DMWJ has been extensively studied. The results showed that the stress and strain fields at crack tip, crack growth paths and *J*-resistance curves were related to the microstructure of DMWJ at different locations [10–12]. When the initial crack located in the base metal or the center of the weld metal, the crack-tip plastic and damage zones were symmetrical, the crack propagated along the initial crack plane and the *J*-resistance curve was high [13]. When the initial crack located in the interface or the near interface zone, the crack-tip plastic and damage zones were asymmetric, the crack growth path had a significant deviation phenomenon and the *J*-resistance curve was lower [14, 15]. When the initial crack located in the fusion line, a symmetrical plastic zone occurred at the crack tip firstly. With the propagation of crack, the plastic zone become asymmetric, and the crack growth path was deflected [16, 17]. When the initial crack located in the heat-affected-zone, the plastic zone was asymmetric, and the crack deviated to the weld interface rapidly [16–18]. Unfortunately, in these studies, the effect of constraint on fracture behavior has not been considered.

On the other hand, much research has been done on the effect of constraint on the local fracture resistance of homogeneous materials, and the fracture mechanics have been developed from single-parameter to the two parameters, three parameters, and the unified parameter which can characterize both in-plane and out-of-plane constraints, as shown in Fig. 1. However, these studies are only focused on the homogeneous material or similar metal welded joint, and the DMWJ with complex microstructures has not been considered.

Only limited studies about the effect of constraint on the local fracture behavior of DMWJ can be found in the literature. Keinanen et al. [19] tested the *J*-resistances of the

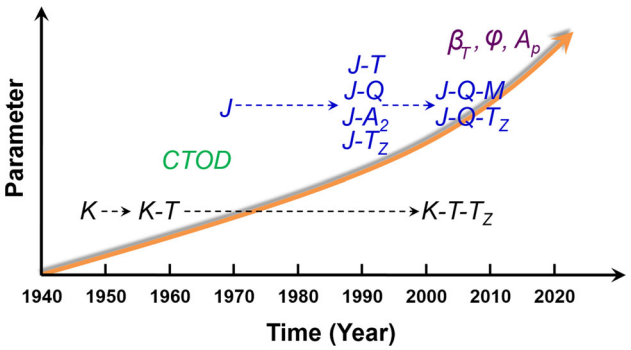

Fig. 1 Development of constraint parameter. Single-parameter: *K*, *CTOD*, *J*; two-parameter: *K*–*T*, *J*–*T*, *J*–*Q*, *J*–A_2, *J*–T_Z; three-parameter: *K*–*T*–T_Z, *J*–*Q*–T_Z, *J*–*Q*–*M*; unified parameter: β_T, φ, A_p

DMWJ with different constraints, Blouin et al. [20] tested a large number of specimens with various types and crack locations at low temperature, and Wang et al. [21] studied the ductile crack growth of a DMWJ with different crack depths. More recently, the authors [22, 23] investigated the effect of constraint on the local fracture resistances of two cracks which located in the weakest regions of an Alloy52M DMWJ by experiment. The results showed that with increasing constraint, the fracture mechanism of the two cracks changed from ductile fracture through mixed ductile and brittle fracture to brittle fracture, and led to the decrease in fracture toughness rapidly. It is dangerous if this change was ignored. Thus, for accurate failure assessment of the DMWJ, the effects of constraint on the fracture behavior of cracks which located in the weakest location of DMWJ need to be investigated systematically.

However, it is time consuming and difficult for a large number of fracture mechanic experiments, and the stress, strain and damage fields at the crack tip during the fracture process cannot be obtained by experiment directly. Fortunately, the local approach based on GTN (Gurson–Tvergaard–Needleman) damage model has been widely used to study the fracture behavior of materials under different constraint conditions successfully [24]. If a set of GTN parameters of the DMWJ were calibrated, the fracture behavior of DMWJ under different constraints can be obtained.

In this work, the two cracks (the crack 2 at A508 HAZ and the crack 3 at A508/52Mb interface, as shown in Fig. 2) which located in the weakest regions of an

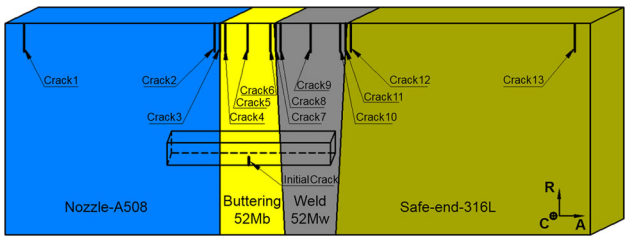

Fig. 2 Materials of the DMWJ and the initial crack positions [8, 13]

Alloy52M DMWJ were selected, and the GTN parameters of DMWJ were calibrated. And then, a micromechanical analysis of in-plane constraint effects on the local fracture behavior of DMWJ was carried out based on GTN damage model.

2 Micromechanical Analysis

2.1 Materials of the DMWJ

In this study, a DMWJ which is used for connecting the safe end to pipe-nozzle of the reactor pressure vessel in NPPs was used. The DMWJ was fabricated by Shanghai Company of Nuclear Power Equipment in China. The pipe-nozzle material was ferritic low-alloy steel (A508) and was supplied in the form of a forging with quenching and tempering treatments. The safe end pipe material was austenitic stainless steel (316L) and was supplied in the form of a solution treated and water-quenched pipe. The weld was manufactured by applying a buttering technique, and the buttering material as well as weld material was the same nickel-base alloy (Alloy52M), but their manufacture procedures were different [8, 13].

To prevent from welding cracking, the base metal A508 was pre-heated to about 125 °C before buttering. The buttering layer was deposited through an Alloy52M welding wire (the diameter of wire is 1.2 mm) by automatic gas-tungsten arc welding (GTAW) on the ferritic nozzle face. The carbon equivalent of the A508 steel is 0.6187%, and its susceptibility to welding cracking is low. The welding current, voltage and speed were 200 A, 11.5 V and 1.85 mm/s, respectively. A total of 478 weld passes were deposited, and the buttering layer with an average width of 20 mm was formed. Then a heat treatment (annealing at 610 °C for 15 h, with subsequent furnace cooling to 300 °C) was conducted on the buttering to relieve the residual stress. After that, 100% non-destructive testing (ultrasonic testing) was performed on the buttering, and no defects were found within the fusion zone and buttering layers. This buttering layer material is denoted as Alloy52Mb [8, 13].

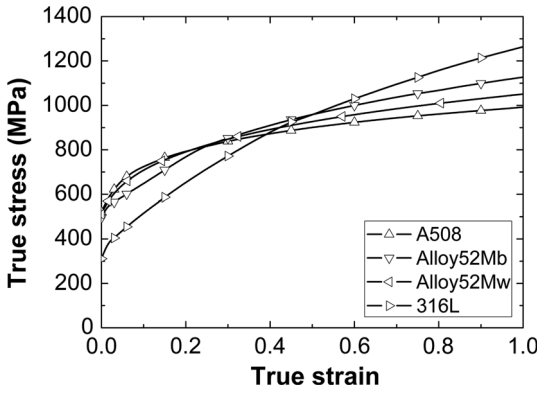

Fig. 3 True stress–strain curves of the four materials at room temperature [25]

After buttering, welding was carried out between the buttering layer and the austenitic safe end pipe using the GTAW and the Alloy52M welding wire (the diameter of wire is 0.9 mm). The welding current, voltage and speed were 180 A, 10 V and 1.75 mm/s, respectively. A total of 439 weld passes were deposited, and the weld with an average width of 19 mm was produced. Here, this weld metal material is denoted as Alloy52Mw. After welding, 100% non-destructive testing (ultrasonic testing) was performed again on the weld, and no defects were found within the welding zone [8, 13].

The materials of the DMWJ are shown in Fig. 2, and the chemical compositions of the materials used for fabrication of the DMWJ are listed in Table 1. The true stress–strain curves of the materials at room temperature are shown in Fig. 3, and the mechanical property data are listed in Table 2 [25].

2.2 Specimen Geometry

The single-edge notched bend (SENB) specimens were used in the finite element method (FEM) analysis. The two weakest positions (the crack 2 and crack 3) with the lowest *J*-resistance curves were selected. The crack 2 is located in the A508 HAZ with a 1.5-mm distance from A508/52Mb interface, and the crack 3 is located in the A508/52Mb interface, as shown in Fig. 2.

Table 1 Chemical compositions of the materials used for fabrication of the DMWJ (wt%)

	C	S	P	Si	Mn	Ni	Cr	Mo	Cu	Al	Ti	Co	Fe	Nb
A508	0.20	0.001	0.005	0.20	1.36	0.96	0.17	0.47	–	–	–	–	Balance	–
52Mb	0.02	<0.001	0.003	0.14	0.25	60.39	28.91	0.01	0.01	0.67	0.56	0.01	9.03	<0.01
52 Mw	0.025	0.001	0.004	0.18	0.24	58	29.18	0.01	0.02	0.75	0.53	0.02	10.23	<0.01
316L	0.025	0.001	0.005	0.52	1.73	11.69	17.89	2.43	–	–	–	–	Balance	–

Table 2 Mechanical property data of the four materials at room temperature [25]

Material	Young's modulus, E (MPa)	Poisson's ratio, v	Yield stress, σ_0 (MPa)
A508	202,410	0.3	514
Alloy52Mb	178,130	0.3	495
Alloy52 Mw	178,130	0.3	511
316L	156,150	0.3	311

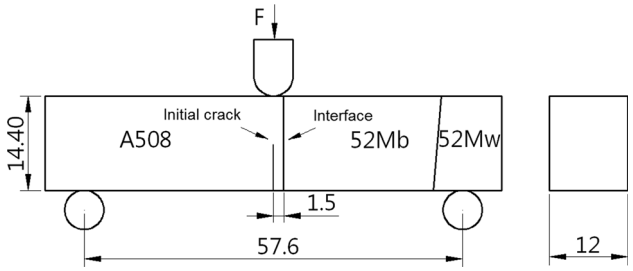

Fig. 4 Loading configuration and geometry of the SENB specimen (for the crack 2 specimen)

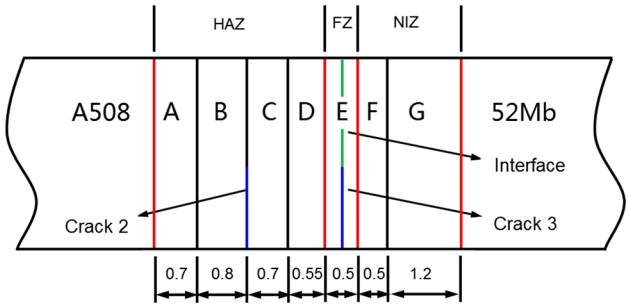

Fig. 5 Multi-material zones in the A508/52Mb interface region

To investigate the fracture behavior of two cracks under different in-plane constraints, the crack 2 and crack 3 specimens with five crack depths (fixed specimen thickness $B = 12$ mm and width $W = 14.4$ mm) denoted as $a/W = 0.2$, 0.3, 0.5, 0.6 and 0.7 were used. The dimensions of these specimens are consistent with the experiments in Ref. [22]. The loading configuration and geometry of the crack 2 specimen are typically illustrated in Fig. 4, the loading point and the initial crack are located in the center of the specimen, and the loading span S is 57.6 mm ($S = 4$ W).

2.3 Local Heterogeneous Mechanical Properties

To incorporate the strength mismatch of A508/52Mb interface region into the finite element models, the interface region was divided into three zones: heat-affected-zone (HAZ) in A508, fusion zone (FZ) and near interface zone (NIZ), as shown in Fig. 5. Furthermore, according to the local microstructure and hardness, the HAZ was further divided into four-material zones (A, B, C and D zones in Fig. 5), the NIZ was divided into two-material zones (F and G zones in Fig. 5) and the FZ is a single-material E zone [6].

The true stress–strain curves of the A, B, C, D, E, F and G zones at room temperature were determined by the mini-sized flat tensile specimens in the work [25] and reproduced in Fig. 6, the elastic modulus E and Poisson's ratio v for the HAZ, FZ and NIZ are taken to be 180,000 MPa and 0.3, respectively. These multi-material zones were modeled in the GTN damage model shown in the next section, and the true stress–strain data of each

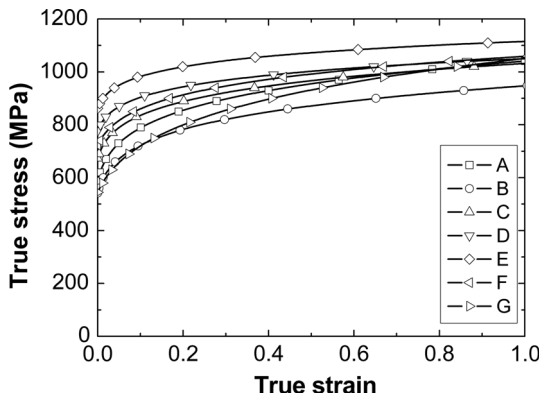

Fig. 6 True stress–strain curves of the multi-materials [6]

zone in Fig. 6 were used in the finite element analyses. For the four materials (A508, Alloy52Mb, Alloy52Mw and 316L) beyond the interface region, the material property data in Fig. 3 and Table 2 were used in the finite element analyses.

2.4 GTN Damage Model and Parameters

One of the most commonly used models for simulating ductile fracture was Gurson constitutive model, in which the effect of void volume fraction is taken into account in the constitutive equations as an extra internal variable. The Gurson model considered material as a homogeneous, uncompressible ideal rigid plastic medium, and used the von Mises plasticity criterion as a yield criterion. The model was modified by Tvergaard and Needleman, Tvergaard later for introducing additional parameters (q_1, q_2,

Table 3 GTN damage parameters

	A508	HAZ	FZ	IAZ	52Mb	52 Mw	316L
q_1	1.5	1.5	1.5	1.5	1.5	1.5	1.5
q_2	1	1	1	1	Variable	1	Variable
q_3	2.25	2.25	2.25	2.25	2.25	2.25	2.25
ε_N	0.3	0.3	0.3	0.3	0.3	0.3	0.3
S_N	0.1	0.1	0.1	0.1	0.1	0.1	0.1
f_N	0.002	0.002	0.008	0.002	0.002	0.002	0.002
f_0	0.00008	0.00015	0.0008	0.00004	0.000001	0.00015	0.000001
f_C	0.04	0.04	0.01	0.04	0.04	0.04	0.04
f_F	0.25	0.25	0.15	0.25	0.25	0.25	0.25

q_3) and a modified damage variable f^*. This is mostly often referred as GTN (Gurson–Tvergaard–Needleman) model. The yield function of the GTN model has the following form:

$$\phi(\sigma_m, \sigma_{eq}, f^*) = \frac{\sigma_{eq}^2}{\sigma_f^2} + 2q_1 f^* \cosh\left(\frac{3q_2\sigma_m}{2\sigma_f}\right) - 1 - q_3 f^{*2} = 0. \quad (1)$$

where σ_m is the hydrostatic stress, σ_{eq} is the von Mises equivalent stress and σ_f is the flow stress of the "voidless" matrix material. The q_1, q_2 and q_3 are phenomenological based parameters, which are used to consider the interaction between adjacent voids. The void volume fraction f^* is the substitute of f in the original equation, which is used to take into account the gradual loss of the stress carrying capability of the material due to void coalescence. The void coalescence occurs when the void volume fraction f reaches the critical value f_c, and the fracture occurs when the f reaches the critical failure void volume fraction f_F. This GTN damage model has been implemented in ABAQUS code as a user material subroutine and is widely used to simulate and predict the crack initiation and propagation. The GTN damage model was used to obtain the crack growth behavior of specimens with different in-plane constraints in this paper.

Generally, the GTN damage model contains nine parameters: q_1, q_2, q_3, f_0, f_N, ε_N, S_N, f_C and f_F. The q_1, q_2 and q_3 are the constitutive parameters, the f_0 is the initial void volume fraction, the f_N, ε_N and S_N are the void nucleation parameters, the f_C is the critical void volume fraction and the f_F is final failure parameter. To simplify the complex calibration process of these parameters, the q_1, q_2 and q_3 are usually fixed to be $q_1 = 1.5$, $q_2 = 1$, $q_3 = q_1^2$, and the values of $\varepsilon_n = 0.3$ and $S_N = 0.1$ have been used in most investigations for low-alloy steels [26]. The parameters f_0, f_N, f_c and f_F are obtained by fitting the numerical J-resistance curves with experiments [26, 27]. The J-resistance curve will increase with decreasing f_0 and f_n and increasing f_c and f_F, and vice versa.

In a recent study, Dutta and Guin [28] pointed out that the variation of the q_2 parameter near the crack tip is helpful to make the numerical J-resistance curves close to the experimental values for various materials. The J-resistance curve and fracture toughness of a material will increase with decreasing q_2. Thus, in this paper, $q_1 = 1.5$, $q_3 = q_1^2$, $\varepsilon_n = 0.3$ and $S_N = 0.1$ were selected, the other parameters (f_0, f_N, f_c, f_F and q_2) were obtained by a comparison of the experimental and numerical J-resistance curves, as shown in Table 3 and Fig. 7.

It should be mentioned that the values of f_c and f_F in the FZ are lower than those in other zones. This is because the J-resistance curve of the FZ is the lowest [13], the decrease in f_c and f_F will reduce the J-resistance curve.

The finite element meshes for the typical crack 2 specimen ($a/W = 0.5$) are illustrated in Fig. 8. The FEM analysis based on GTN model is explicit and dynamic, and the mesh sizes of 0.1 mm × 0.05 mm were used in the crack growth regions [24]. The typical model contains 72,608 elements and 84,105 nodes. The loading was applied at the top and center of the SENB specimen by prescribing a displacement of 6 mm.

The load versus load-line displacement curves can be obtained from the FEM simulations. With instantaneous crack length obtained at each loading point, the J-curves can be determined in reference to the resistance curve procedure, as specified in ASTM E1820.

3 Results and Discussion

3.1 *J*-Resistance Curves

Figure 9 shows the comparison of J-resistance curves which were obtained from the experiments in Ref. [22] and the numerical simulations in this paper. It can be seen that the numerical J-resistance curves are consistent with the experiment results, which shows that the GTN model can incorporate the in-plane constraint effect.

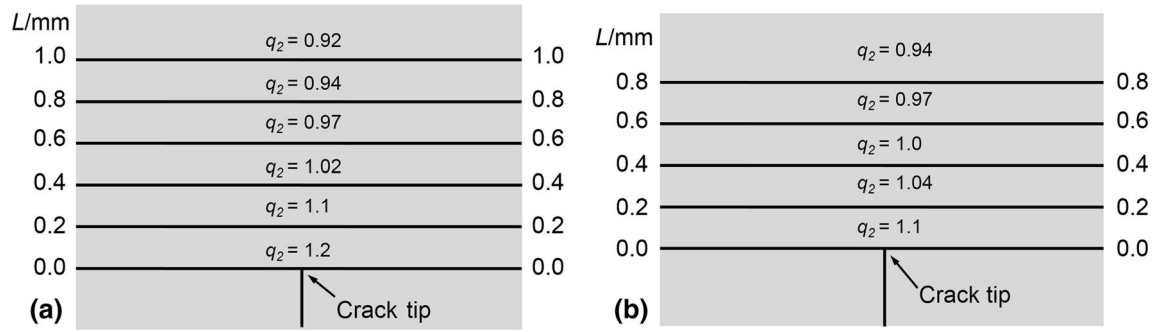

Fig. 7 Distributions of q_2 along the distance L from crack tip: **a** 52Mb, **b** 316L

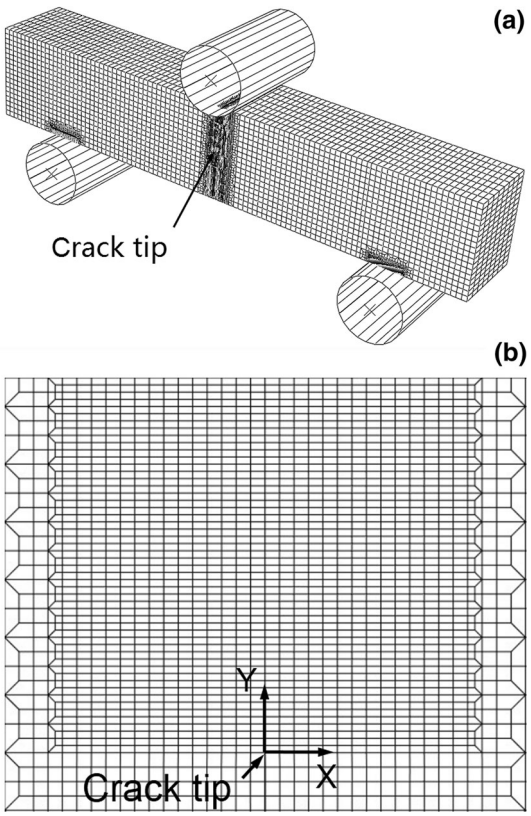

Fig. 8 Meshes of the whole model **a**, meshes along the crack growth area **b**

It can also be found that the J-resistance curves of the two cracks decrease with increasing in-plane constraint. The specimens with the lowest in-plane constraint ($a/W = 0.2$) have the highest J-resistance curves, while the specimens with the highest in-plane constraint ($a/W = 0.7$) have the lowest J-resistance curves. The reason will be analyzed in Sect. 3.3.

3.2 Crack Growth Paths

The crack growth paths of the crack 2 specimens which were obtained from the experiments in Ref. [22] and the numerical simulations in this paper are shown in Fig. 10. It can be found that the numerical crack growth paths are consistent with the experiment results, which indicates that the GTN damage parameters are accurate and efficient, and can be used to obtain the crack growth paths of specimens with different in-plane constraints.

Furthermore, it can also be found that when the crack depth $a/W = 0.2$, the crack growth path is nearly straight along the initial crack plane. The irregular crack edges on the crack growth path are characteristics of void ductile fracture [29]. When the crack depth $a/W = 0.5$, the crack has a deviation path toward A508 base metal whose strength is lower than that of A508 HAZ. The smooth crack edges at the beginning of crack growth path are characteristics of brittle fracture. When the crack depth $a/W = 0.7$, the crack has a deviation path toward A508 base metal strongly. All of the crack edges are smooth and sharp, which means that the brittle fracture occurs here.

Figure 11 shows the crack growth paths of the crack 3 specimens with different in-plane constraints which were obtained from the experiments in Ref. [22] and the numerical simulations in this paper. It can be found that the numerical crack growth paths are consistent with the experiment results also.

Furthermore, it can also be found that when the crack depth $a/W = 0.2$, the crack is nearly straight along the interface firstly [30] and then tends to deviate to the side of 52Mb with lower strength. The fracture surface is rough and scraggly, which implies that substantial energy has been consumed to separate the crack surface, the fracture mechanism is highly ductile fracture. When the crack depth $a/W = 0.5$, the crack has a deviation path toward the side of 52Mb with lower strength, and the crack edges are serrated. When the crack depth $a/W = 0.7$, the crack has a deviation path toward 52Mb strongly. The fracture surface is smooth, which means the fracture mode is brittle fracture in this specimen.

The results in the previous study of authors have shown that the fracture mechanism of crack 2 and crack 3

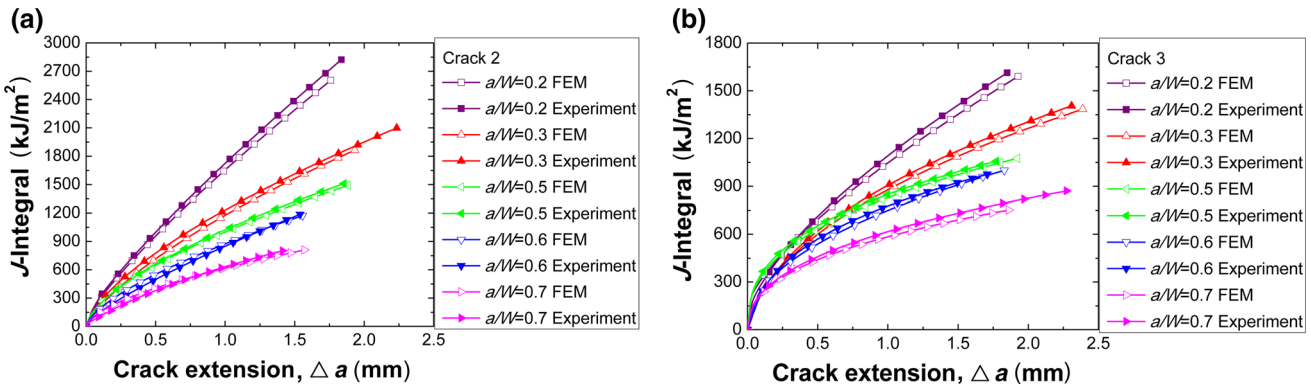

Fig. 9 Comparison of the experimental and numerical *J*-resistance curves for the specimens with different in-plane constraints: **a** crack 2, **b** crack 3

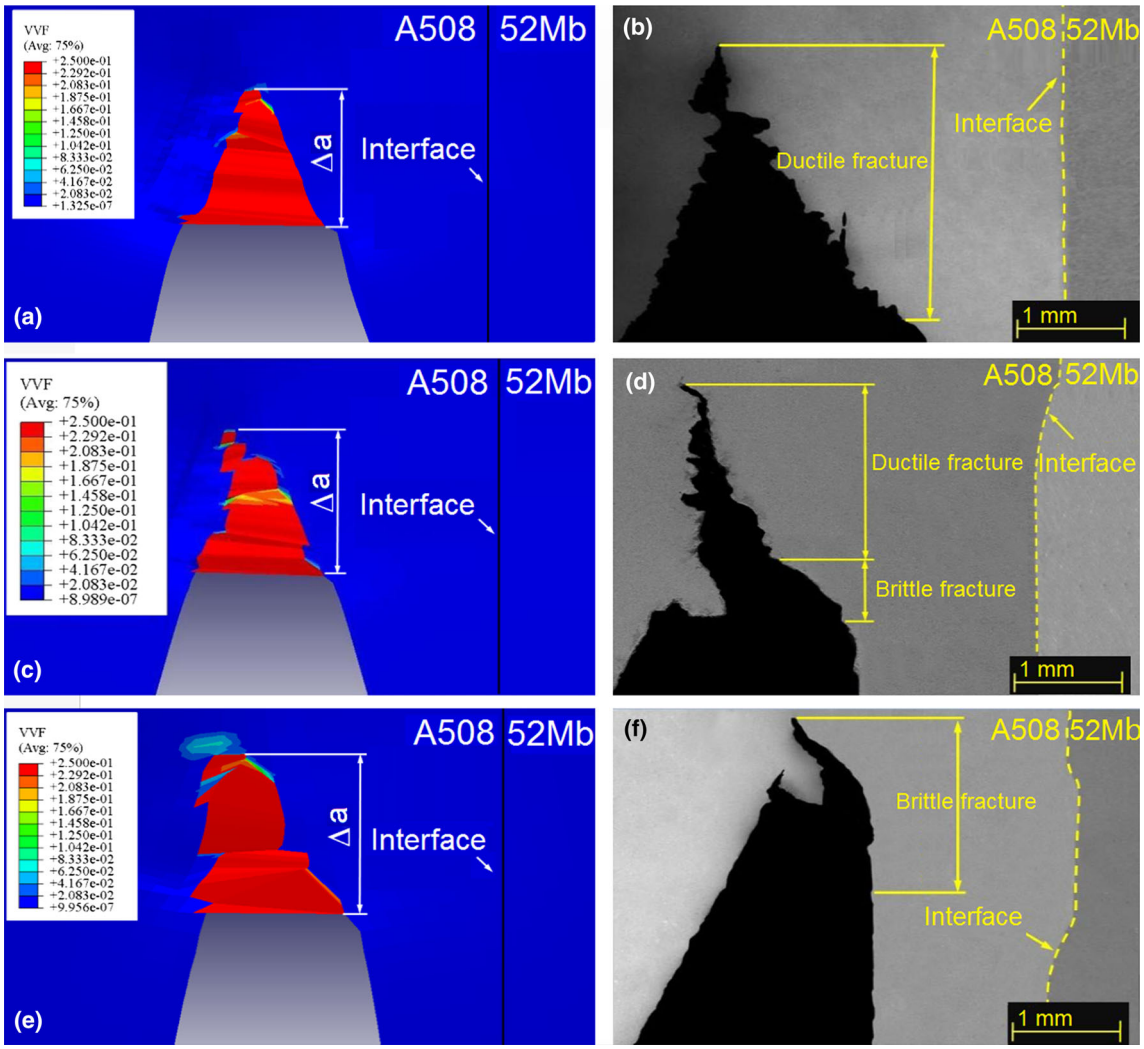

Fig. 10 Crack growth paths obtained from the numerical simulations **a**, **c**, **e** and the experiments **b**, **d**, **f** for crack 2 specimens with $a/W = 0.2$ **a**, **b**, $a/W = 0.5$ **c**, **d** $a/W = 0.7$ **e**, **f**

specimens are ductile when the in-plane constraint is low. With increasing in-plane constraint, the fracture mechanism changes from ductile fracture through mixed ductile and brittle fracture to brittle fracture [22]. It is consistent with the characteristic of crack growth paths in this paper, the reason will be analyzed in Sect. 3.3.

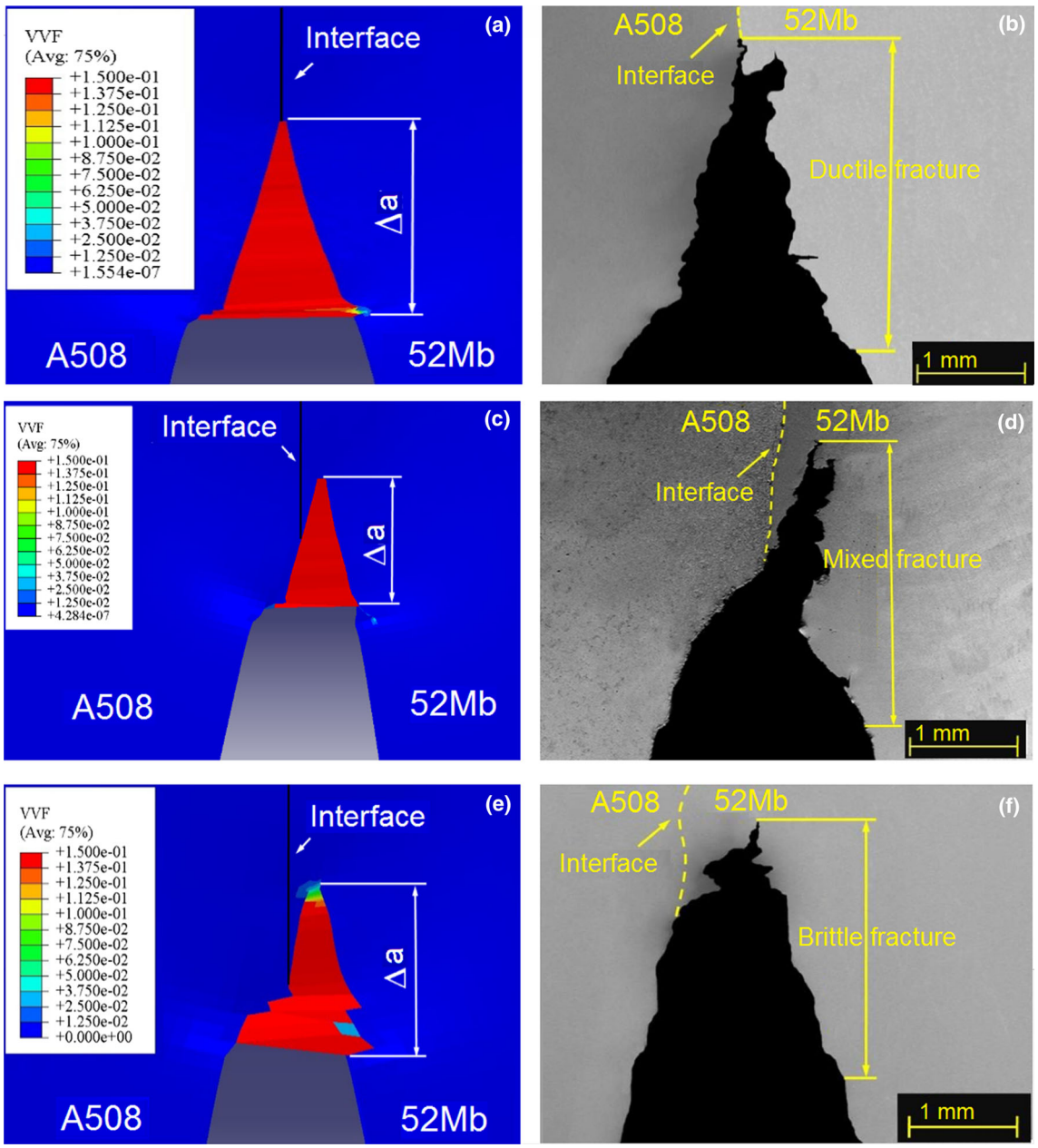

Fig. 11 Crack growth paths obtained from the numerical simulations **a**, **c**, **e** and the experiments **b**, **d**, **f** for crack 3 specimens with $a/W = 0.2$ **a**, **b**, $a/W = 0.5$ **c**, **d** $a/W = 0.7$ **e**, **f**

3.3 Micromechanical Analysis of In-Plane Constraint Effect on Fracture Behavior

3.3.1 PEEQ, VVF, TRIAX and S of Specimens with Different In-Plane Constraints at the Same J-Integral

Figure 12 shows the PEEQ (equivalent plastic strain), VVF (void volume fraction), TRIAX (stress triaxiality) and S (Mises stress) of crack 2 specimens with different in-plane constraints at the same J-integral ($J = 200$ kJ/m^2). The PEEQ reflects the local plastic deformation at crack tip, the VVF reflects the damage of material, the TRIAX and S reflect the stress state at crack tip. The micromechanical analysis of the crack 2 and crack 3 specimens reflects the similar results, thus, only the results of crack 2 specimens were listed here.

It can be seen clearly that the PEEQ and VVF increase with increasing in-plane constraint. It means that the same load will promote larger plastic deformation and longer

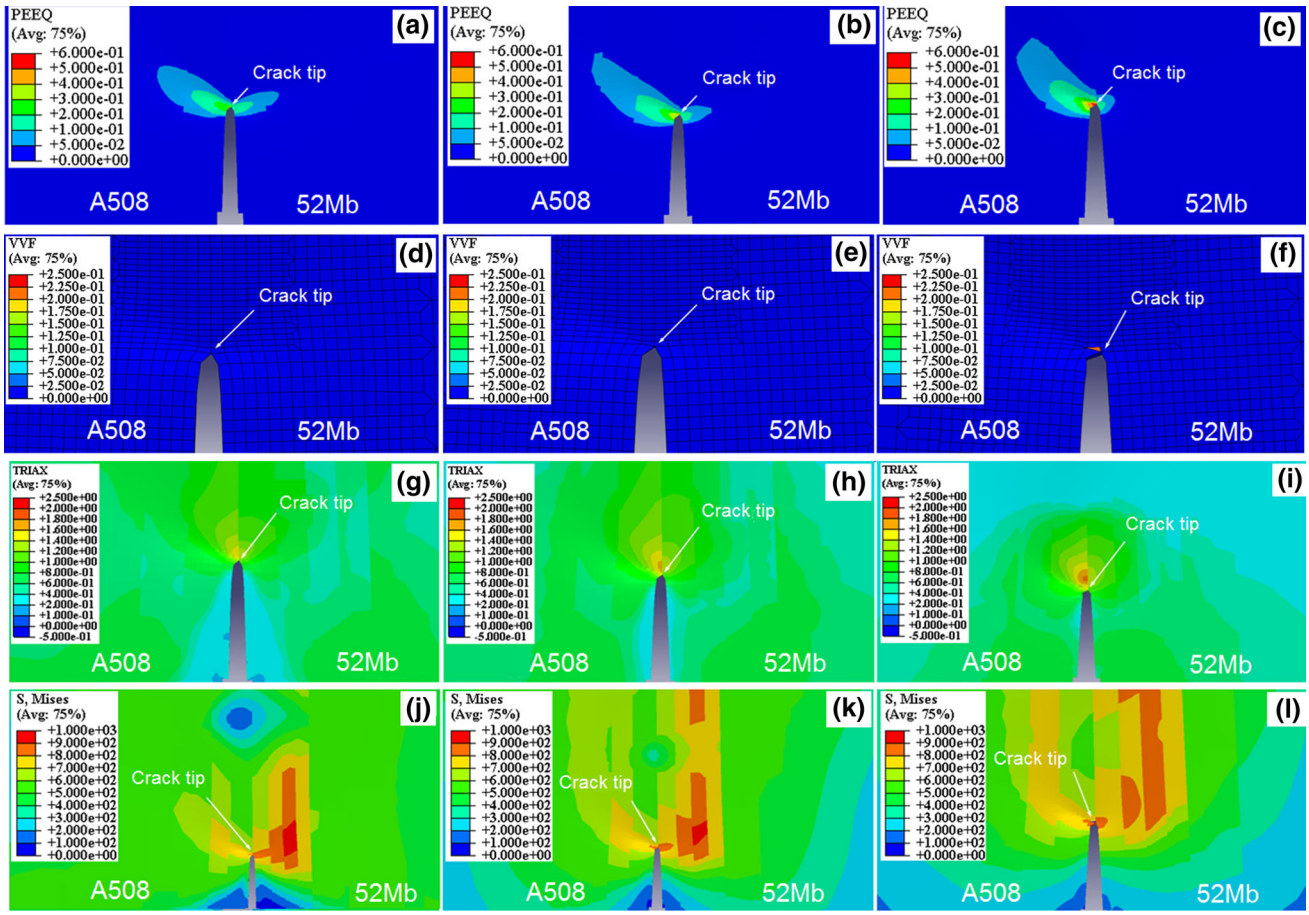

Fig. 12 PEEQ, VVF, TRIAX and S of crack 2 specimen with $a/W = 0.2$ **a**, **d**, **g**, **j**, $a/W = 0.5$ **b**, **e**, **h**, **k**, $a/W = 0.7$ **c**, **f**, **i**, **l** at $J = 200$ kJ/m^2

propagation in specimen with higher in-plane constraint. The specimen with higher constraint has the lower fracture resistance and will fracture more easily. Thus, the J-resistance curve of specimen decreases with increasing in-plane constraint. The specimen with $a/W = 0.2$ (the lowest constraint in this paper) has the highest J-resistance curve, while the specimen with $a/W = 0.7$ (the highest constraint in this paper) has the lowest J-resistance curve, as shown in Fig. 9.

It can also be found that at the same J-integral, the TRIAX at crack tip increases with increasing in-plane constraint. For the high TRIAX can promote the initiation and propagation of brittle fracture or lower ductile fracture [31–33], the trend and percentage of brittle fracture will increase with increasing in-plane constraint, as described in Sect. 3.2. The specimen with $a/W = 0.2$ which has the lowest TRIAX is favorable for the development of ductile fracture.

The large plastic deformation relaxes the stress at the crack tip, thus, the magnitude of S decreases with increasing in-plane constraint. This is consistent with the Ref. [34], which showed that the stress is lower in the specimen with high constraint under the same load.

Furthermore, it can be found that the PEEQ, VVF, TRIAX and S are heterogeneous at the crack tip because of the effect of strength mismatch. The PEEQ, VVF and TRIAX at the left side of the crack tip (A508 base metal with lower strength) are larger than those at the right side (A508 HAZ). With increasing in-plane constraint, the heterogeneity became more obvious. This is why the crack has a deviation path toward A508 base metal, and the deviation will become stronger under higher in-plane constraint.

3.3.2 The PEEQ, VVF, TRIAX and S of the Crack 2 Specimen with a/W = 0.5 at Different J-Integrals

Figure 13 shows the PEEQ, VVF, TRIAX and S of the crack 2 specimen with $a/W = 0.5$ at different J-integrals. It can be seen that the crack has not yet begun to expand (the VVF < 0.25 at crack tip) at $J = 200$ kJ/m^2 (lower J-integral). The PEEQ and TRIAX are lower, while the S at the crack tip is higher. The distributions of PEEQ, VVF, TRIAX and S are asymmetric, the PEEQ, VVF and TRIAX mainly occur in the material of A508, while the S mainly

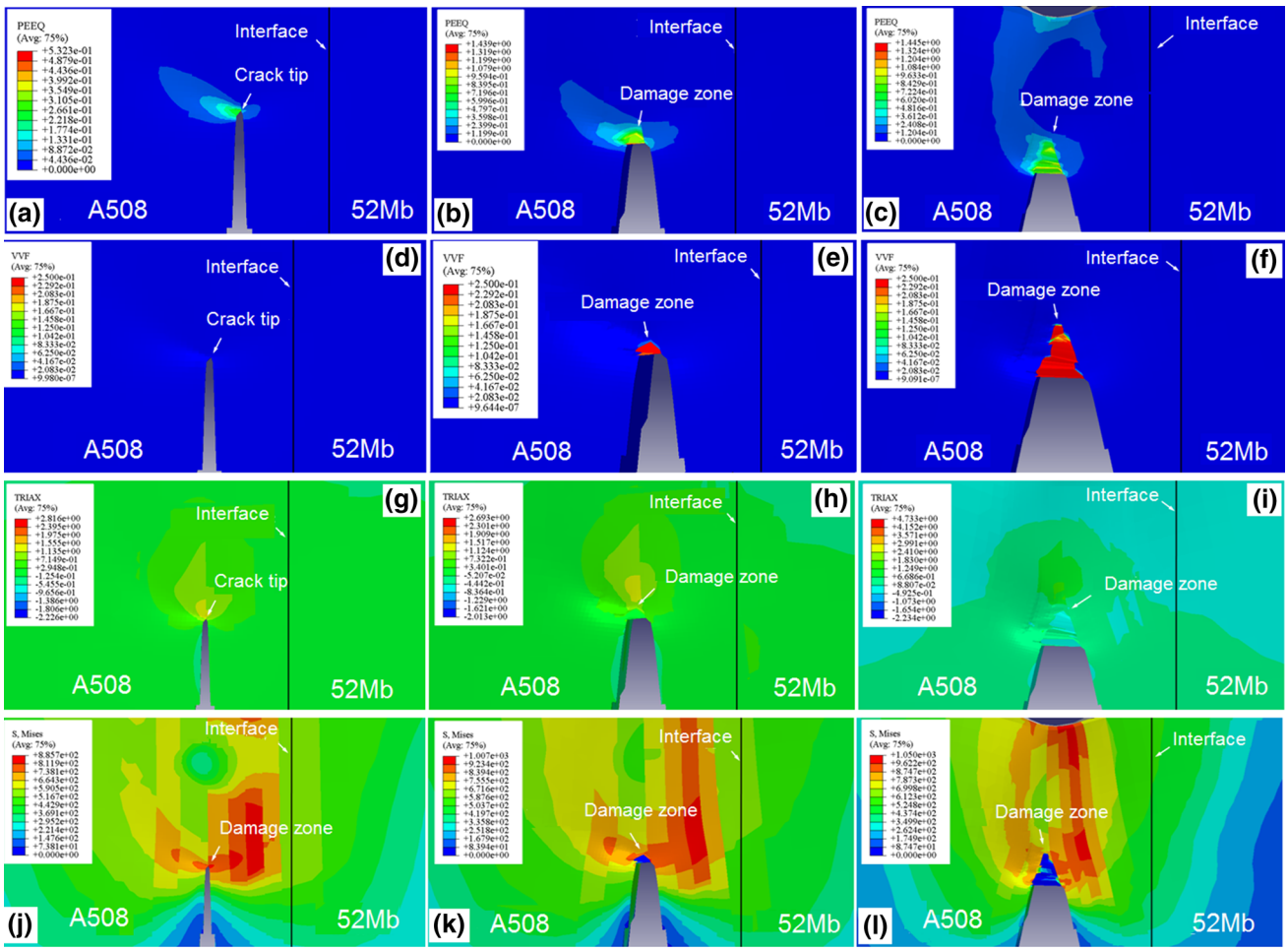

Fig. 13 PEEQ, VVF, TRIAX and S of the crack 2 specimen with $a/W = 0.5$ at $J = 200$ kJ/m^2 **a**, **d**, **g**, **j**, $J = 500$ kJ/m^2 **b**, **e**, **h**, **k** and $J = 1200$ kJ/m^2 **c**, **f**, **i**, **l**

occurs in the material of 52Mb. For the crack located in the A508 HAZ with higher strength martensite microstructure but low fracture toughness, the brittle fracture will occur under higher S.

With increasing J-integral, the crack propagates a short length at $J = 500$ kJ/m^2. The PEEQ and the TRIAX increase under higher load, while the S at the crack tip decreases. The distributions of PEEQ, VVF, TRIAX and S are asymmetric. The PEEQ, VVF and TRIAX mainly occur in the material of A508, while the S mainly occurs in the material of 52Mb also.

When the $J = 1200$ kJ/m^2, the crack has a long propagation and toward to the A508 base metal during the propagation process. The crack path deviation will promote the change of fracture mechanism from brittle fracture to the ductile fracture. This comes from two factors. One factor is that the crack path deviation makes the mode I crack change into mixed crack of modes I and II, and this reduces the driving stress for brittle fracture. The other factor is that the crack path deviates to the material with lower strength, and larger plastic deformation may relax local crack-tip opening stress, which can promote the development of ductile fracture process. Therefore, the local brittle fracture firstly initiates and propagates from the initial fatigue pre-crack tip, and then changes into ductile fracture, as shown in Fig. 10c, d.

In summary, these results suggest that the fracture behavior of cracks, such as J-resistance, crack growth path and fracture mechanism, in the weakest locations of DMWJ are complex and sensitive to the in-plane constraint. For accurate and reliable failure assessment of the DMWJ structures, it needs to consider the effect of in-plane constraint on fracture behavior. The local approach based on GTN damage model is an effective method to study the fracture behavior of DMWJ under different in-plane constraints.

4 Conclusions

1. A set of GTN parameters of the Alloy52 M DMWJ were calibrated in this work. The partition of the material according to local microstructure and hardness and the variation of the q_2 parameter will help the *J*-resistance curves close to the experimental values.
2. The *J*-resistances and crack growth paths of the specimens obtained from numerical simulations are consistent with the experiment results. The *J*-resistance, crack growth path and fracture mechanism are sensitive to the in-plane constraint and relate to the stress, strain and damage fields at crack tip.
3. The local approach based on GTN damage model can be used to consider the effect of in-plane constraint on the fracture behavior of DMWJ.

Acknowledgements This work is supported by the National Natural Science Foundation of China (Grant No. 51605292), the Natural Science Foundation of Shanghai (Grant No. 15ZR1429000) and the Youth Foundation of Shanghai (Grant No. ZZslg15013).

References

[1] A.R. Mcllree, in *PWR Material Reliability Project, Part 1: Alloy82/182 Pipe Butt Welds*, EPRI Report TP-1001491 (2001)
[2] R. Celin, F. Tehovnik, Mater. Technol. **45**, 151 (2011)
[3] A. Jenssen, K. Norrgard, J. Lagerstron, *Assessment of Cracking in Dissimilar Metal Welds*. Paper presented at the 10th international symposium on environmental degradation of materials in nuclear power systems-water reactors, USA (2001)
[4] S. Farley, *An Overview of Non Destructive Inspection Service in Nuclear Power Plants*. Paper presented at the international conference nuclear energy for New Europe, Slovenia, 6–9 Sept 2004
[5] International Atomic Energy Agency, Laea. Vienna, Austria (2009)
[6] H.T. Wang, G.Z. Wang, F.Z. Xuan, C.J. Liu, S.T. Tu, Mater. Sci. Eng., A **568**, 108 (2013)
[7] Y. Wu, Y. Cai, H. Wang, S.J. Shi, X.M. Hua, Y.X. Wu, Mater. Des. **87**, 567 (2015)
[8] H.T. Wang, G.Z. Wang, F.Z. Xuan, S.T. Tu, Eng. Fail. Anal. **28**, 134 (2013)
[9] W. Brocks, W. Schmitt, The second parameter in *J-R* curves: constraint or triaxiality. ASTM STP 1244 (1995). doi:10.1520/STP14637S
[10] M.K. Samal, K. Balani, M. Seidenfuss, E. Roos, P. I. MECH. ENG. C-J. MEC. **223**, 1507 (2009)
[11] C. Faidy, *Structural Integrity of Dissimilar Welds: ADIMEW Project Overview*. Paper presented at ASME/JSME pressure vessels & piping conference, San Diego, California, USA, 25–29 July 2004
[12] H. Xue, K. Ogawa, T. Shoji, Nucl. Eng. Des. **239**, 628 (2009)
[13] H.T. Wang, G.Z. Wang, F.Z. Xuan, S.T. Tu, Mater. Des. **44**, 179 (2013)
[14] M.K. Samal, M. Seidenfuss, E. Roos, K. Balani, Eng. Fail. Anal. **18**, 999 (2011)
[15] K. Fan, G.Z. Wang, F.Z. Xuan, S.T. Tu, Eng. Fract. Mech. **136**, 279 (2015)
[16] R. Chhibber, N. Arora, S.R. Gupta, B.K. Dutta, P. I. MECH. ENG. C-J. MEC. **220**, 1121 (2006)
[17] A. Laukkanen, P. Nevasmaa, U. Ehrnsten, R. Rintamaa, Nucl. Eng. Des. **237**, 1 (2007)
[18] Y.B. Shang, H.J. Shi, Z.X. Wang, G.D. Zhang, Mater. Des. **88**, 598 (2015)
[19] H. Keinanen, E. Keim, K.R. Paivi, S. Blasset, P.Gilles, T. Nicak, *Results of EC FP7 Structural Performance of MULTI-METAL Component Project: Dissimilar Metal Welds Fracture Resistance Investigation*. Paper presented at ASME pressure vessels & piping conference, Boston, Massachusetts, USA, 19–23 July 2015
[20] A. Blouin, S. Chapuliot, S. Marie, C. Niclaeys, J.M. Bergheau, Eng. Fract. Mech. **131**, 58 (2013)
[21] H.T. Wang, G.Z. Wang, F.Z. Xuan, S.T. Tu, Nucl. Eng. Des. **241**, 3234 (2011)
[22] J. Yang, G.Z. Wang, F.Z. Xuan, S.T. Tu, C.J. Liu, Mater. Des. **53**, 611 (2014)
[23] J. Yang, G.Z. Wang, F.Z. Xuan, S.T. Tu, C.J. Liu, Mater. Des. **55**, 542 (2014)
[24] E. Østby, C. Thaulow, Z.L. Zhang, Eng. Fract. Mech. **74**, 1771 (2007)
[25] H.T. Wang, G.Z. Wang, F.Z. Xuan, C.J. Liu, S.T. Tu, Adv. Mater. Res. **509**, 103 (2012)
[26] N. Benseddiq, A. Imad, Int. J. Press. Vessels Pip. **85**, 219 (2008)
[27] I. Penuelas, C. Betegon, C. Rodrıguez, Eng. Fract. Mech. **73**, 2756 (2006)
[28] B.K. Dutta, S. Guin, Int. J. Press. Vessels Pip. **85**, 199 (2008)
[29] Y.G. Deng, H.S. Di, J.C. Zhang, Acta Metall. Sin. (Engl. Lett.) **28**, 1141 (2015)
[30] Z.J. Yan, X.S. Liu, H.Y. Fang, Acta Metall. Sin. (Engl. Lett.) **29**, 1161 (2016)
[31] G.Z. Wang, J.H. Chen, J.G. Wang, Int. J. Fract. **118**, 211 (2002)
[32] J.H. Chen, Q. Wang, G.Z. Wang, Z. Li, Acta Mater. **51**, 1841 (2003)
[33] G.Z. Wang, Y.L. Wang, Int. J. Fract. **146**, 105 (2007)
[34] F. Wang, W.C. Cui, Acta Metall. Sin. (Engl. Lett.) **1**, 41 (2010)